Three-Terminal Junctions operating as mixers, frequency doublers and detectors: A broad-band frequency numerical and experimental study at room temperature

I. Iñiguez-de-la-Torre[1,4], T. González[1], D. Pardo[1], C. Gardès[2], Y. Roelens[2], S. Bollaert[2], A. Curutchet[3], C. Gaquiere[2] and J. Mateos[1]

[1]*Departamento de Física Aplicada, Universidad de Salamanca, Plaza de la Merced s/n, 37008 Salamanca, Spain*

[2]*Institut d'Electronique de Microélectronique et de Nanotechnologie (IEMN), Avenue Poincaré BP 69, 59652, Villeneuve d'Ascq CEDEX, France*

[3]*Laboratoire IMS, Université Bordeaux 1, 351 Cours de la Libération, 33405 Talence, France*

[4]*Present address: Department of Electrical and Computer Engineering, University of Massachusetts, Lowell, MA 01854 USA*

E-mail: indy@usal.es

Abstract: The frequency response of nanometric T- and Y-shaped three-terminal junctions (TTJs) is investigated experimentally and numerically. In virtue of the parabolic down-bending of the output voltage of the central branch obtained at room temperature under a push-pull fashion input, we analyze: the low-frequency performance (<1 MHz) of TTJs operating as mixers, their RF capability as doublers up to 4 GHz and detection at 94 GHz. Special attention is paid to the impedance matching and cut-off frequency of the measurement set-up. The numerical study is done by means of Monte Carlo simulations. We illustrate the intrinsic functionality of the device as frequency doubler or rectifier up to THz. The role of the width of the central branch on the high-frequency response is also explored, finding different cut-off frequencies for doubling and detection as a consequence of the diverse working principles of both mechanisms and the particular geometry of the TTJs.

I. INTRODUCTION

In modern electronics the miniaturization for present lithographic processes is reaching the nanometre size. At this scale, devices are based on novel working principles, in which surface and quantum effects play a key role on their final behaviour. Within this frame, nanodevices based on semiconductor heterostructures called Three Terminal Junction (TTJ) [1, 2] are emerging as potential building blocks of analog and digital integrated circuits. The III-V heterostructure creates a high mobility 2DEG layer in which electrons can move overcoming very few scattering events. This ballistic or quasiballistic transport of electrons inside the devices and their particular geometry (T- or Y-shaped) provoke an attractive and robust nonlinear response of TTJs confirmed by theory [3], numerical simulations [4] and experiments [5]. Therefore, the use of high electron mobility InGaAs channels with high indium content (providing mobilities in excess of 10.000 cm^2/Vs at 300 K, with the advantage of being compatible with advanced HEMT technology) is key for improved operation of these devices at room temperature. Another advantage of TTJs in comparison with conventional devices arises from its small size, which allows a high integration density and a high intrinsic operation speed.

Several possible applications of TTJs have been demonstrated by different authors: rectification up to 94 GHz at room temperature [6], frequency doubling in the range of 20 MHz-1 GHz [7] and logic circuits as a NAND gate [8], a half-adder [9] or a set-reset (SR) latch [10]. Similarly GaAs-based three terminal nanowires junctions controlled by Schottky wrap gates (WPGs) [11] are known to operate as Boolean gates [12]. Also recently, power gain at room temperature up to 1.5 GHz has been measured in TTJs [13], remarkably demonstrating their capability to act as active devices. Frequency mixing at low-frequency [14] has also been measured, but with significant signal decay, attributed to a mismatching problem. Finally, Monte Carlo (MC) simulations have shown that ballistic nanodevices can have intrinsic cut off frequencies above 1 THz [15]. Understanding the limits of the dynamic performance of TTJs will be the objective of this paper since not much effort has been put till now to study the response of TTJs at very high-frequency, approaching the THz range.

This paper describes our study, both experimental and numerical, of the frequency performance of TTJs operating as mixers, doublers and detectors in several frequency bands, ranging from a fraction of kHz to 94 GHz, and with different experimental setups. All measurements and simulations are performed at room temperature. The paper is organized as follows. In section II we provide a brief description of the fabrication process, simulation method and working principle of TTJs. Section III describes how the device operates as a mixer at low-frequency (<1 MHz). This low-frequency experiment will be used to illustrate the influence of the equipment on the effective cut-off frequency of the mixing setup. Then, frequency doubling and phase detection will be demonstrated at an intermediate frequency of 4 GHz. To conclude with the experimental work we will show how an

optimized structure with reduced parasitics can operate as a detector at much higher frequencies, experimentally reaching 94 GHz (limit of the equipment). The possibility of intrinsic operation (parasitic capacitances, accesses and cables are not included in simulations) at frequencies approaching the THz range is finally explored by means of Monte Carlo simulations. Also the influence of the width of the vertical stem of the TTJ is analyzed. Finally section V draws the most important conclusions of this work.

II. EXPERIMENTAL, SIMULATION METHOD AND DEVICE OPERATION PRINCIPLE

II.1 TTJ Fabrication process

The InGaAs/InAlAs heterostructure on which the fabricated TTJ is based was grown by Molecular Beam Epitaxy (MBE) at the IEMN [16]. An indium content of 75% in the InGaAs channel is used in order to obtain high electron mobility (10.000 cm^2/Vs) and sheet electron density ($2.65x10^{12}$ cm^{-2}). The geometry of the TTJ is defined with a high resolution negative resist, Hydrogen SilsesQuioxane exposed by electron beam lithography with a Leica EBPG5000+, followed by dry etching with a $CH_4/H_2/Ar$ plasma. This solution has been preferred to wet etching because it provides a lower edge roughness and a better control of undercut. A Ni-Ge-Au-Ni-Au metal sequence is then deposited by evaporation and is annealed at 300°C with a N_2H_2 gas to form the ohmic contacts. Finally, Ti-Au bonding pads are evaporated.

II.2 Monte Carlo simulator

The Monte Carlo simulations, based on a semiclassical transport description, allows to get a detailed insight into the processes taking place inside the devices, thus allowing the determination of the optimum topologies of the TTJs for high-frequency applications. Our MC simulator is self-consistently coupled with a 2D Poisson solver [17]. The model contains all the necessary ingredients for the correct modelling of ballistic devices such as: accurate models for ionized impurity, alloy, polar and nonpolar optical phonon, acoustic phonon and intervalley scattering, consideration of Γ-L-X nonparabolic spherical valleys and appropriate carrier injection techniques at the contacts. Surface charges appearing at the semiconductor interfaces with dielectrics (crucial when the size is reduced up to the nano-scale) are also self-consistently included in the simulations [18]. When analyzing the response of TTJs at very high-frequency (section IV), the profile of the surface charge used in the simulation is *frozen* to that previously calculated under equilibrium conditions, since the typical capture/emission times of the surface states are about 1 μs, several orders of magnitude longer than the maximum period used for exciting the TTJ (1 ns). This approximation is in good agreement with recent simulations of the role played by dynamically adapted surface charges at these high-frequencies [19, 20].

Even if the structures under analysis would require 3D simulations to exactly reproduce their topology, a 2D simulator has been used. The limitations of this simulator have been overcome by performing "front-view" and "top view" consistent simulations [21]. This work focuses in top view simulations in which the real layer structure is not included, and only the high mobility channel with its special geometry (playing a key role) will be simulated. More details of the simulations can be found in the references [4, 21]. The validity of this approach has been successfully checked in previous works by means of the comparison with experimental results [18, 22, 23], predicting excellent high-frequency performances for ballistic nanodevices, in some cases reaching the THz range [15, 24]. In addition, our approach has recently been further validated by the results of Sadi *et al.* [19]. Using a 3D model (including our self-consistent model to incorporate surface charge effects) they have almost perfectly replicated the results obtained with our 2D model for the same set of TBJ junctions [18].

II.3 Device operation principle

Our device consists in three branches connected with T- or Y-shape geometry. In big devices, where the mean free path (ℓ_m) is smaller that the distance between contacts, each branch can be represented by a resistance [Fig. 1(a)]. So, if we apply two separate potentials with opposite sign to the right and left terminals (push-pull fashion), the potential in the middle of the junction is zero. In this ohmic transport regime, the potential measured at the bottom of the open-circuited central branch (stem), V_C, is also zero [Fig. 1(c)]. However, when the lengths of the branches, L, are smaller than the mean free path, transport can not be anymore considered diffusive, but ballistic or quasiballistic. In this regime, the horizontal branches can be considered as non-linear resistances $R(V)$ [25], Fig. 1(b), and as shown by the experiments [1, 2, 5] and theory [26], V_C is always negative and varies quadratically with the input $V_C=-\alpha V^2+O(V^4)$, Fig. 1(c). The origin of this phenomenon has been explained by means of MC simulations [4, 18], and it is related to the asymmetric profile of electron concentration along the horizontal branches, being higher near the negative electrode due to (i) ballistic transport and (ii) an asymmetric distribution of surface charges. This property of TTJs can be exploited to perform several analog and digital functions such as mixing [14], frequency doubling [7, 27], high-frequency detection [6], NAND [8, 12] or NOR gates [28], etc.

It is important to remark that, as sketched in Fig. 1(c), when increasing the bias (V>0.5 V), even in the ballistic TTJs, the response of V_C becomes linear with V due to the appearance of intervalley scattering mechanisms, that lead to the emergence of an accumulation domain near the positive electrode completely screening the variation of the potential drop between the central branch and the negative electrode [5, 22]. This mechanism is also responsible for the saturation of the current and the surprising negative values of V_C (since they are expected to be ohmic) measured in large size TTJs [5, 22]. Another important feature of the TTJ behaviour is that, contrary to the expectations, the central

branch is not exactly a potential probe which measures the potential at the middle of the TTJ. Instead, surface charge effects at the stem boundaries provoke that the potential drop along the vertical branch is not equal for all the biasings, so that the value of V_C is not a direct transmission of the potential at the centre of the TTJs, and therefore depends on the stem width [18].

As a summary, we can state that the nonlinearities of these devices can be explained in terms of the broken device symmetry as a result of inhomogeneous electron concentration given by a complex mix of electron ballistic transport and surface-charge effects. Finally, the robustness of the TBJ's nonlinear response observed in experiments over a wide range of channel sizes [5, 22, 23, 29] is a unique advantage in terms of realizing room-temperature integrated circuitry using TBJs.

III. MEASUREMENTS

This section describes several experiments that investigate the dynamic response of the TTJs in a broad frequency range, being the ultimate goal the integration into THz nanosystems. This nanoscale devices can reach extremely high-frequencies of operation mainly because of the small electron transit time (as a result of the ballistically high electron velocity). However, due to the small width of the channels, TTJs show relatively high impedances, ranging from few kΩ to MΩ. From the point of view of circuit design this poses a serious problem of impedance mismatching when driving the load. So first we will show, for frequency mixing and relatively low-frequencies (<1MHz) how the experimental set-up can distort the characterization process.

With a correct design of the coplanar waveguide accesses to the active region of the TTJ, the crosstalk capacitances, parasitic resistances and mismatching effects can be minimized. In the second subsection two experiments at much higher frequencies (4 and 94 GHz) showing those improvements are shown. However, even for a combination of low capacitive coupling between input and output electrodes (cross talk capacitances around 1 fF) and relative low impedance (around 1 kΩ) the cut-off frequency estimated from the RC time is still very low, about 160 GHz, so that other approaches should be foreseen if aiming to the THz range (for example the use of multichannel structures [11]).

III.1 Mixing

Mixers are essential components for telecommunication applications. Heterodyne mixers are present in all modern receivers. A device with nonlinear response is essential to obtain at the output a combination of the frequencies of the two input signals. The well known parabolic response found in the output voltage of TTJs (measured at the open circuited bottom branch) under push-pull bias (of the left and right branches) offers the possibility to fabricate frequency mixers in which both the original input frequencies and their sum and difference will be displayed at the output. In order to demonstrate this capability we apply two sinusoidal signals with the same amplitude A and different frequencies f_1 and f_2, $V_1=A\cos(2\pi f_1 t)$ and $V_2=A\cos(2\pi f_2 t)$, to the left and right branches of a TTJ, respectively, as

sketched in the top left inset of Fig. 2. As the static response of the TTJ can be approximated by V_C=-αV^2+bV+c, where α is the curvature of the response, b represents the asymmetry of the junction and c is a constant accounting for the offset of the setup, with V the push-pull input voltage, V_1-V_2=2V, the stem voltage V_C should show a value:

$$V_C = -\alpha\left(\frac{V_1 - V_2}{2}\right)^2 + \frac{V_1 + V_2}{2} + b\frac{V_1 - V_2}{2} + c. \qquad (1)$$

The term $(V_1+V_2)/2$ must be also considered to include the effect of the offset of the input bias. From this expression it is easy to obtain that the amplitude of the output spectral components in our case should be: $\alpha A^2/4+c$ for DC, $A(1+b)/2$ for f_1, $A(1-b)/2$ for f_2, $\alpha A^2/4$ for f_1+f_2 and f_2-f_1, and $\alpha A^2/8$ for $2f_1$ and $2f_2$. We will check the presence of this frequency spectrum in measurements performed in a T-shaped nanojunction with 180 nm wide and 250 nm long horizontal branches, and a 90 nm wide vertical branch. This TTJ has firstly been characterized in static conditions. The potential at the bottom of the central branch and the current in the horizontal branch measured with an HP Agilent 4142B modular DC source when biasing left and right branches in push-pull is represented in Fig. 3. The fitting to V_C=-αV^2+bV+c in the range ±100 mV (that covered by the mixing experiment) is also shown in the figure, with α=5.7 V^{-1}, b=-0.124, c=1.8 mV.

Next, the experimental setup of Fig. 2 is used to verify the mixing response of the TTJ. All measurements are performed at room temperature and in darkness. The right inset of Fig. 2 represents the equivalent circuit of the measurement setup. R_{os} is the input impedance of the oscilloscope, R_{TTJ} the output impedance of the junction, C_{cab} the capacitance of the cables and the rest of equipment and V_m the measured potential. The equivalent circuit simply shows that, at zero frequency V_m is given by $V_C\times R_{os}/(R_{os}+R_{TTJ})$. When the frequency of the input signals increases, the $R_{os}C_{cab}$ network of the equipment causes a decay in the measured potential. In order to estimate the TTJ output impedance, R_{TTJ}, the resistances between each two contacts (the third contact is open circuited) have been measured, giving the following values R_1=3.7 kΩ and R_2=R_3≈1 MΩ. Then, by a simple mathematical conversion (following the scheme of Fig. 3), the resistance of each branch is obtained: R_C=1 MΩ and R_A=R_B=1.85 kΩ, thus providing a value for $R_{TTJ}=R_C+R_A||R_B$ of around 1 MΩ. To determine the cut-off frequency, f_c, associated with the capacitance of the external cables, the amplitude at the output has been measured leaving open one of the inputs and applying a 100 mV sinusoidal signal of increasing frequency to the other. The estimated f_c is about 6 kHz, as observed in Fig. 4, that using the expression $f_c=1/(2\pi R_{os}C_{cab})$ since the device capacitances are very low (of the order of fF), provides a value for C_{cab} of 26 pF, which is completely reasonable, bearing in mind that we are employing a fraction of meter of cables of 40-80 pF/m. The impedance of the oscilloscope used for the measurements is R_{os}=1 MΩ, so that at low-frequency the measured potential V_m is about half of V_C.

Fig. 5 shows the comparison of the response predicted by Eq. (1) using the parameters obtained from the fitting of the static V_C-V curve, with the measurements of frequency mixing for different

values of the amplitude (A) and frequencies (f_1 and f_2) of the input signals. In order to obtain the spectrum of the output signal, a discrete Fast Fourier Transform (FFT) based on the Cooley-Tukey algorithm [23] is applied to the time domain data of the oscilloscope. In the analytical results, the influence of R_{TTJ}, the decay associated to the pole (we divide the spectra by $1+f/f_c$) and a factor 2 because of the Fourier transform (having sense only for positive frequencies) have been included in the calculation of V_C. Fig. 5(a) corresponds to A=100 mV, f_1=500 Hz and f_2=600 Hz. The measured spectrum is well reproduced by the analytical model, exhibiting all the spectral components with amplitudes of 6.18 mV for DC, 3.48 mV for f_2-f_1, 12.97 mV for f_1, 9.95 mV for f_2, 1.52 mV for $2f_1$, 2.99 mV for f_1+f_2 and 1.47 mV for $2f_2$. The agreement in the time domain (inset) response is also excellent. Similar results can be observed in Fig. 5(b) for f_2=50 Hz.

If we increase the frequency of the excitation, the attenuation introduced by the measuring equipment ($R_{os}C_{cab}$ network) provokes a notable decrease in the amplitude of the harmonics. To avoid it, we have reduced the oscilloscope input impedance to R_{os}=100 kΩ. In this way the characteristic frequency of the pole is raised by a factor of ten to 60 kHz. The drawback is that now R_{TTJ} is one order of magnitude higher than R_{os}, and so the signal is attenuated by a factor of 11 even at low-frequency. In Fig. 6, corresponding to f_2=19.3 kHz, these features can be observed. Again we have the different harmonics: $2f_1$=1 kHz, f_2-f_1=18.8 kHz and f_1+f_2=19.8 kHz.

Finally, the device has been measured under a higher amplitude of the input signals, A=200 mV, results shown in Fig. 7 for f_1=500 Hz and f_2=600 Hz. In this case, the previously used quadratic expression is not adequate to correctly fit the static V_C-V curve of the TTJ in the whole range covered. So, we propose a higher-order polynomial expression such as:

$$V_C = A + BV + CV^2 + DV^3 + EV^4. \qquad (2)$$

By using this new equation (within the ±200 mV range) the best fit to the measurements, shown in Fig. 7(a), is obtained with A=-0.74 mV, B=-0.11, C=-6.5 V^{-1}, D=4.8 V^{-2} and E=49 V^{-3}. Under these conditions some new harmonics (with respect to the case shown in Fig. 5(a) for a lower amplitude of the inputs) appear in the spectrum of the output signal, Fig. 7(b): $2f_2$-f_1=400 Hz and $2f_1$-f_2=700 Hz (V^3 type response), $2(f_2$-$f_1)$=200 Hz, $3f_2$-f_1=900 Hz, $3f_1$-f_2=1300 Hz, $3f_2$+f_1=2100 Hz, $2(f_1$+$f_2)$=2200 Hz and $3f_1$+f_2=2300 Hz (V^4 type response). Even if the analytical curve does not show some of the harmonics the agreement is still quite satisfactory, illustrating the almost ideal mixing operation of the TTJ. Remarkably, these results clearly demonstrate that the frequency limitation of the mixing operation is due to the experimental setup; no degradation due to the intrinsic device response is observed (in [9] surface effects were suggested as a source of high-frequency decay of the output).

III.2 Doubling and detection

In this section we report experimental results illustrating the functionalities of TTJs as frequency doublers and detectors. First, we measure a single YBJ with 250 nm long and 190 nm wide horizontal

branches and 80 nm wide vertical branch with integrated coplanar waveguide accesses, sketched in Fig. 8(a), whose static V_C-V response is shown in Fig. 8(b). To characterize the device acting as frequency doubler and phase detector at high-frequency, a experimental setup combining a Large Signal Network Analyzer (LSNA) with a continuous wave source (Agilent Technologies E8257D PSG) for HF signal generation reaching 20 GHz and coaxial cables for the connections of the source and on-wafer probes is used (more details of the experimental setup can be found in [11]). The measurements are made using high impedance probes (HIP Picoprobe model 35), with impedance of 1.25 MΩ, close to the MΩ impedance range typical of TTJ, thus allowing precise time domain measurements. After adequate calibration steps, the phase and magnitude of the injected (a_1 and a_2) and reflected (b_1 and b_2) waves at the input and output of the device are used to determine the currents and voltages in the frequency or time domain. In Fig. 8(c) an excellent frequency doubling for an input signal of 4 GHz can be observed: a quasi sinusoidal signal at 8 GHz is obtained at the output. The spectrum shown in Fig 8(d) confirms that the second harmonic is the highest in the output. In order to check the possibility of phase detection, signals with same amplitude and three different phase-shifts φ [$V_1=A\cos(2\pi ft)$ and $V_2=A\cos(2\pi ft+\varphi)$] have been applied to the right and left branches. The results of these measurements, shown in Fig. 8(e), are in a very good agreement with the theoretical prediction that can be obtained from eq. (1).

In the particular case of input power detection, in order to further decrease the input impedance and improve the frequency response of the TTJs, we use a double Y-shaped junction defined by means of reactive ion etching on a typical InP-HEMT epilayer and integrated in parallel in a coplanar waveguide. The width of the stem is 200 nm and the angle between the two 220 nm long horizontal branches is around 60º. The complete frequency characterization of the structure between 3 and 40 GHz was presented in [20]. The set-up for the experimental characterization of the RF-DC conversion at 94 GHz is shown in Fig. 9, where a push-fix input (one branch is biased while the other is grounded [3]) originates a DC component in V_C. Fig. 9 shows that the junction is still perfectly operative as detector at such high-frequency, with a measured sensitivity of 76 mV/mW (without DC bias). The linear dependence is a proof of the square-law dependence of the YBJ output (V_C=-αV^2). A real improvement is obtained with respect to the 4 mV/mW at 50 GHz provided by the four-terminal ballistic rectifier [24], and is comparable with the 75 mV/mW obtained with self-switching diodes (SSD) at 110 GHz [25]. However, this sensitivity is still far away from the typically ranges of 4000 mV/mW at 100 GHz to 400 mV/mW at 900 GHz of Schottky diode detectors [26].

The main improvement achieved here with respect to previous works [20] is the optimization of the ohmic contacts accesses and coplanar waveguide design in order to minimize extrinsic crosstalk capacitances without excessively increasing access resistances. Poor matching of high-impedance TTJs and 50 Ω equipment is one of the main problems of these ballistic nanodevices. The use of multiple channels is proposed as a solution for improvement of conversion losses [11].

IV. MONTE CARLO RESULTS

As shown in the previous section, the lack of techniques able to test the pico-second response of TTJs restrains us to their study by means of numerical models. First, it is necessary to better understand the underlying physics of the dynamic operation of the devices and, second, to estimate the intrinsic frequency limits that we can expect in ideal conditions. For this purpose we make use of the MC tool previously described in section II.2 to simulate, at room temperature, the response of TTJs in the sub-millimetre frequency range.

IV.1 Doubling *vs.* detection

The performance of TTJs as frequency doublers or power detectors in the sub-THz range, though not measured experimentally, can be checked (intrinsically) by our MC simulator. To this end, we apply 100 mV sinusoidal signals in push-pull fashion to a T-shaped TTJ with 250 nm long-120 nm wide horizontal branches and a 60 nm wide vertical branch and calculate the bottom potential V_C output for different excitation frequencies. In Fig. 10 the time domain evolution of the stem output voltage V_C is represented when the frequency of the input signal is 1, 10 and 100 GHz and the *frozen* surface charge model is utilized. It can be observed that the device has an excellent performance as frequency doubler at least up to 100 GHz. The static response of the same device is represented in Fig. 11. Two models for the surface charge are used here: self-consisted surface charge model (SSCM) [13] and *frozen* to equilibrium surface charge model [15]. The quadratic fitting for both models are also plotted in the graph. The more negatives values obtained from the self-consistent model are due to the bias re-adaptation of surface charge within this model [18]. From the static behaviour we expect an average output DC value of:

$$\overline{V_C} = f\int_0^{1/f} -\alpha\left[V_0\cos(2\pi ft)\right]^2 dt = -\alpha V_0^{\,2}/2. \qquad (3)$$

For an amplitude V_0 of 100 mV the parabolic fitting of the static response provides an average V_C value of $\overline{V_C}$ =-12.5 mV for the simulations with *frozen* surface charges (using α= -2.5 V^{-1}). In Fig. 10 it can be observed that the time domain average value obtained with the MC simulations using the frozen model (assuming that the characteristic time of the surface states is much slower than the input signal, in agreement with the results shown in Ref. [15]) is in good agreement with this estimation. For input signals of much lower frequencies (when surface charges are able follow the input), the values obtained for $\overline{V_C}$ would be much more negative (for the SCCM model α= -4.2 V^{-1} so that $\overline{V_C}$ =-21 mV). In fact, this could be a possibility to experimentally determine their characteristic lifetime, since a low-frequency plateau should be observed, with a cut-off corresponding to the inverse of such time.

For the detailed dynamic study of the TTJs, sinusoidal signals of 0.1 V amplitude are applied to the left and right branches in push-pull fashion, while monitoring the value of V_C. The amplitude of its response, V_{Cac}, informs about the capability of operating the TTJs as frequency doublers, while the average DC value of V_C, $\overline{V_C}$, provides the rectification performance. Both quantities are plotted in dB in Fig. 12. Due to the quasi-ballistic motion of electrons within the active region of the TTJ, average velocities as high as 5×10^7 cm/s are reached. Therefore, the cut-off frequency of the 560 nm long TTJ presented before should be around 1 THz (associated just to the longitudinal transport). However, while the cut-off frequency of $\overline{V_C}$ is higher than 1 THz, in the case of V_{Cac} the decay appears at much lower frequency, about 50 GHz. This different frequency response appears because rectification (and thus detection) is mainly related to horizontal transport, which is very fast, while the AC amplitude (and thus frequency doubling) is strongly controlled by the penetration of carriers into the central branch. Since the electric field that forces electrons to enter/leave the vertical branch following the excitation signal is small, the characteristic time of such a process is much longer than the transit time associated to horizontal transport, so that the cut-off frequency for V_{Cac} is much lower than in the case of the DC value. We can double-check this conclusion studying the dependence of the results on the value of the width of the vertical branch, which we perform in next section.

IV.2 Influence of the geometry: stem width and junction shape

In this section we study the effect of the geometry on the performance of the TTJs. For T-shaped junctions like the one shown in Fig. 13(a) we consider two parameters to analyze their influence on the dynamic response: the width of the horizontal branches W_{HOR} and the width of the vertical stem W_{VER}. Also, we examine the effect of the junction shape by simulating a Y-shaped device, as drawn in Fig. 13(b).

Figure 14 shows the typical down bending value of V_C and the current flowing through the horizontal branches in all the simulated junctions. When the width of the vertical branch is reduced, the parabolicity in the bell-shape of the V_C-V curves is enhanced, while providing a similar current (as expected since W_{HOR} is the same [13]). A narrower horizontal branch leads to less negative values of V_C (and obviously to lower current). This result is not consistent with the static experimental measurements (shown in Ref. 18), which show more negative values of V_C due to the bias dependence of the surface charge profile. This effect is not considered here, since we focus on the dynamic response of these devices, thus making use of a *frozen* surface charge profile calculated under equilibrium conditions. On the other hand, the stem voltage values are more negative in the Y-shaped junction than in the T-shaped one because of the enhanced electron penetration into the vertical branch [16].

Fig. 15 shows the values of V_{Cac} and $\overline{V_C}$ as a function of frequency for the different simulated TTJs (for the sake of clarity the low-frequency value has been subtracted). As a general feature, the cut-off

for $V_{Cac,}$ Fig. 15(b), appears at much lower frequencies than for the mean value, Fig. 15(a), taking place around 1 THz. As the value of $\overline{V_C}$ is mainly related to the electron horizontal transport, its cut-off is hardly influenced by the width of the vertical branch. On the other hand, V_{Cac} is controlled by the penetration of carriers into the stem, so that its width (W_{VER}) clearly changes its cut-off frequency (higher frequencies for wider stems, in which carriers enter more easily). Nevertheless, wider stems provide less negative values of V_C at low-frequency, as observed in Fig. 14(a). As a consequence, for an optimized response W_{VER} must be chosen depending on the required type of operation and frequency. On the other hand, when reducing the width of the horizontal branch (W_{HOR}), a slight increase of the cut-off frequency is observed in both quantities; however, the matching to the typical 50 Ω lines would be worse due to the higher impedance of the TTJ. Concerning the shape, the Y geometry much improves the global performance of the device as a result of an enhanced vertical electric field and a stronger injection of carriers into the stem (having a more pronounced influence on the cut-off of V_{Cac}, associated with frequency doubling applications). Moreover, better performances are expected if the angle between left and right branches of the junction is further decreased. However, if the size of the device is reduced below the Fermi wavelength of the electrons and the temperature is decreased so that the scattering is negligible, the wave nature of the electron transport may come into sight, thus making the sensitivity and cut-off frequency of the TTJs become insensitive to the size of the stem channel as well as the angle between the left and right branches [26].

V. CONCLUSIONS

In this paper we have experimentally demonstrated the operation of TTJs as mixers, doublers and detectors based on the presence of ballistic or quasiballistic transport. Mixing at low-frequency and low amplitude shows an output voltage containing components (apart from DC) at the original input frequencies, and their sum and difference. For higher amplitudes new harmonics appear due to the non-parabolic response of the device. A simple analytical study shows that due to the high value of the TTJ output impedance (of the order of kΩ), considerably larger than the desired value of 50 Ω of the standard high-frequency experimental equipment, special attention to the impedance matching and cut-off frequency of the measurement set-up is essential. For higher frequencies, signal detection up to 94 GHz and frequency doubling and phase detection up to 4 GHz have been experimentally confirmed in a double Y-shaped junction.

By means of MC simulations, we have shown that, at least intrinsically, TTJs are good candidates for building devices capable of operating up to 100 GHz as frequency doublers and even entering the THz range as detectors. The reduction of the stem width increases the sensitivity in the static response but reduces the cut-off frequency for doubling. Nevertheless the detection capabilities are not much deteriorated and a negative value is obtained even for sub-millimetre wave frequencies.

This results shows that the robustness of the TTJ's nonlinear response is a unique advantage in terms of realizing room temperature circuits working at ultra high-frequencies. In order to confirm the theoretical expectations, experimental techniques able to probe the electrical properties of these nanodevices at terahertz frequencies (>100 GHz to 10 THz) are necessary. To this end a promising picosecond electrical measurement set-up has been recently proposed [24]. However, aspects related to the fabrication process, reliability and particularly interconnects still have to be investigated in order to use TTJs for room temperature applications that can give us access to the THz range.

ACKNOWLEDGMENTS

This work has been partially supported by the European Comission through the ROOTHz Project ICT-2009-243845, by the Dirección General de Investigación (MEC) and FEDER through Project TEC2007-61259/MIC and by the Consejería de Educación, Junta de Castilla y León through Projects SA019A08 and GR270.

REFERENCES

[1] Worschech L, Xu H Q, Forchel A and Samuelson L 2001 Bias-voltage-induced asymmetry in nanoelectronic Y-branches *Appl. Phys. Lett.* **79** 3287

[2] Shorubalko I, Xu H Q, Maximov I, Omling P, Samuelson L and Seifert W 2001 Nonlinear operation of GaInAs/InP-based three-terminal ballistic junctions *Appl. Phys. Lett.* **79** 1384

[3] Xu H Q 2002 Diode and transistor behaviors of three-terminal ballistic junctions *Appl. Phys. Lett.* **80** 853

[4] Mateos J, Vasallo B G, Pardo D, González T, Galloo J S, Roelens Y, Bollaert S and Cappy A 2003 Ballistic nanodevices for terahertz data processing: Monte Carlo simulations *Nanotechnology* **14** 117

[5] Irie H, Diduck Q, Margala M, Sobolewski R and Feldman M J 2008 Nonlinear characteristics of T-branch junctions: Transition from ballistic to diffusive regime *Appl. Phys. Lett.* **93** 053502

[6] Bollaert S, Cappy A, Roelens Y, Galloo J S, Gardès C, Teukam Z, Wallart X, Mateos J, González T, Vasallo B G, Hackens B, Berdnarz L and Huynen I 2007 Ballistic nano-devices for high frequency applications *Thin Solid Films* **515** 4321

[7] Lewén R, Maximov I, Shorubalko I, Samuelson L, Thylén L and Xu H Q 2002 High frequency characterization of a GaInAs/InP electronic waveguide T-branch switch *J. Appl. Phys.* **91** 2398

[8] Xu H Q, Shorubalko I, Wallin D, Maximov I, Omling P, Samuelson L and Seifert W 2004 Novel Nanoelectronic Triodes and Logic Devices With TBJs *IEEE Electron Device Lett.* **25** 164

[9] Worschech L, Reitzenstein S, Hartmann P, Kaiser S, Kamp M and Forchel A 2003 Self-switching of branched multiterminal junctions: a ballistic half-adder *Appl. Phys. Lett.* **83** 2462

[10] Sun J, Wallin D, Maximov I and Xu H Q 2008 A Novel SR Latch Device Realized by Integration of Three-Terminal Ballistic Junctions in InGaAs/InP *IEEE Electron Device Lett.* **29** 540

[11] Nakamura T, Kasai S, Shiratori Y and Hashizume T 2009 Fabrication and characterization of a GaAs-based three-terminal nanowire junction device controlled by double Schottky wrap gates *Appl. Phys. Lett.* **90** 102104

[12] Rahman S F B A, Nakata D, Shiratori Y and Kasai S 2009 Boolean logic gates utilizing GaAs three-branch nanowire junctions controlled by Schottky wrap gates *Jpn. J. Appl. Phys.* **48** 06FD01

[13] Spanheimer D, Müller C R, Heinrich J, Höfling S, Worschech L and Forchel A 2009 Power gain up to gigahertz frequencies in three-terminal nanojunctions at room temperature *Appl. Phys. Lett.* **95** 103502

[14] Sun J, Wallin D, Brusheim P, Maximov I, Wang Z G and Xu H Q 2007 Frequency mixing and phase detection functionalities of three-terminal ballistic junctions *Nanotechnology* **18** 195205

[15] Vasallo B G, González T, Pardo D and Mateos M 2004 Monte Carlo analysis of four-terminal ballistic rectifiers *Nanotechnology* **15** S250

[16] Gardès C. 2008 *Composants nanométriques balistiques de la filière InGaAs/InAlAs/InP pour applications hautes fréquences* (Doctoral Thesis : L'Université des Sciences et Technologies de Lille)

[17] Jacoboni C and Lugli P 1989 *The Monte Carlo method for semiconductor device simulation* (New York: Springer-Verlag)

[18] Iñiguez-de-la-Torre I, Mateos J, González T, Pardo D, Galloo J S, Bollaert S, Roelens Y and Cappy A 2007 Influence of the surface charge on the operation of ballistic T-branch junctions: a self-consistent model for Monte Carlo simulations *Semicond. Sci. Technol.* **22** 663

[19] Sadi T, Dessenne F and Thobel J 2009 Three-dimensional Monte Carlo study of three-terminal junctions based on InGaAs/InAlAs heterostructures *J. Appl. Phys.* **105** 053707

[20] Sadi T and Thobel J 2009 Analysis of the high-frequency performance of InGaAs/InAlAs nanojunctions using a three-dimensional Monte Carlo simulator *J. Appl. Phys.* **106** 083709

[21] Mateos J, Vasallo B G, Pardo D, González T, Galloo J S, Bollaert S, Roelens Y and Cappy A 2003 Microscopic modeling of nonlinear transport in ballistic nanodevices *IEEE Trans. Electron Devices* **50** 1897

[22] Mateos J, Vasallo B G, Pardo D, González T, Pichonat E, Galloo J S, Bollaert S, Roelens Y and Cappy A 2004 Nonlinear effects in T-branch junctions *IEEE Electron Device Lett.* **25** 235

[23] Iñiguez-de-la-Torre I, González T, Pardo D, Gardès C, Roelens Y, Bollaert S and Mateos J 2009 Influence of the branches width on the nonlinear output characteristics of InAlAs/InGaAs-based three-terminal junctions *J. Appl. Phys.* **105** 094504

[24] Iñiguez-de-la-Torre I, Mateos J, Pardo D, Song A M and González T 2009 Noise and THz rectification linked by geometry in planar asymmetric nanodiodes *Appl. Phys. Lett.* **94** 093512

[25] Bednarz L, Rashmi, Hackens B, Farhi G, Bayot V and Huynen I 2005 Broad-band frequency characterization of double Y-branch nanojunction operating as room-temperature RF to DC rectifier *IEEE Trans on Nanotechology* **4** 576

[26] Xu H Q 2001 Electrical properties of three terminal ballistic junctions *Appl. Phys. Lett.* **78** 2064

[27] Shorubalko I, Xu H Q, Maximov I, Nilsson D, Omling P, Samuelson L and Seifert W 2002 A Novel Frequency-Multiplication Device Based on Three-Terminal Ballistic Junction *IEEE Electron Device Lett.* **23** 377

[28] Müller C R, Worschech L, Höpfner P, Höfling S and Forchel A 2007 Monolithically integrated logic NOR gate based on GaAs/AlGaAs three-terminal junctions *IEEE Electron Device Lett.* **28** 859

[29] Wallin D, Shorubalko I, Xu H Q and Cappy A 2006 Nonlinear electrical properties of three-terminal junctions *Appl. Phys. Lett.* **89** 092124

[30] Cooley J W and Tukey J W 1967 An algorithm for the machine calculation of complex Fourier series *Math. Comput.* **19** 297

[31] Song A M, Omling P, Samuelson L, Seifert W, Shorubalko I and Zirath H 2001 Operation of InGaAs/InP-based ballistic rectifiers at room temperature and frequencies up to 50 GHz *Jpn. J. Appl. Phys.* **40**, L909

[32] Balocco C, Song A M, Åberg M, Forchel A, González T, Mateos J, Maximov I, Missous M, Rezazadeh A A, Saijets J, Samuelson L, Wallin D, Williams K, Worshech L and Xu H Q 2005 Microwave detection at 110 GHz by nanowires with broken symmetry *Nano Letters* **5**, 1423

[33] Hesler J. L. and Crowe T. W. 2007 Responsivity and Noise Measurements of Zero-Bias Schottky Diode *Proc. of the 18th Intl. Symp. Space Terahertz Techn.* p. 89

[34] Irie H and Sobolewski R 2010 Terahertz electrical response of nanoscale three-branch junctions *J. Appl. Phys*. **107**, 084315

FIGURE CAPTIONS

FIG. 1. Sketch of the (a) ohmic and (b) ballistic regimes of transport in TTJs and the (c) V_C response for both types of transport.

FIG. 2. Experimental setup for the analysis of frequency mixing. The TTJ situated in the probe station is excited by two Tektronix CFG 250 waveform generators. The output is measured by a Tektronix TDS3012 oscilloscope. A simple circuit representation of the measurement setup is shown in the right inset.

FIG. 3. Static V_C-V and I-V characteristics measured in the TTJ under analysis, sketched in the top-left corner. The analytical fitting for V_C is also plotted. Right panel: representation of the resistances measured between contacts R_1, R_2, R_3, and the resistances of each branch R_A, R_B, R_C. The conversion between both sets is given by: $R_1=R_A+R_B$, $R_2=R_A+R_C$ and $R_3=R_B+R_C$.

FIG. 4. Voltage gain in dB of the TTJ of Fig. 3 as a function of the frequency f of the applied signal. V_{out} is calculated as the amplitude of the signal found at the bottom of the central branch when a voltage $V=V_{in}\cos(2\pi ft)$ is applied to one of the horizontal branches and the other is left open (V_{in}=100 mV). The cut-off frequency is estimated by fitting the MC results to a $1/(1+f/f_c)$ decay.

FIG. 5. Frequency and time (inset) domain response of the TTJ of Fig. 3 as measured with the oscilloscope and obtained from the analytical model, respectively, for A=100 mV, f_1=500 Hz and (a) f_2=600 Hz, (b) f_2=50 kHz.

FIG. 6. Frequency and time (inset) domain response of the TTJ of Fig. 3 as measured with the oscilloscope and obtained from the analytical model, respectively, for A=100 mV, f_1=500 Hz and f_2=19.3 kHz.

FIG. 7. (a) Experimental measurements and analytical fitting for V_C within the ±200 mV range and (b) frequency and time (inset) domain response of the TTJ as measured with the oscilloscope and obtained from the analytical model, respectively, for A=200 mV, f_1=500 Hz and f_2=600 Hz.

FIG. 8. (a) Sketch of the Y-shaped TTJ with CPW accesses for the measurements and (b) its static V_C-V characteristic. Time domain response obtained with the LSNA at 4 GHz working as (c) frequency doubler with a 5dBm input signal [its harmonic spectrum is shown in (d)] and (e) phase detector (output for signals with different phase-shift between inputs).

FIG. 9. Detected DC value of V_C *vs*. microwave (94 GHz) power injected to the double Y-shaped junction with V_{bias}=0. The experimental set-up used for the measurements and the static results for V_C are shown as insets.

FIG. 10. Time domain response of V_C in a T-shaped TTJ to push-pull input signals of amplitude 100 mV and frequency (a) 1 GHz, (b) 10 GHz and (c) 100 GHz. The mean value of V_C (around -15 mV, constant with frequency) is shown as red horizontal lines.

FIG. 11. Static V_C-V and I-V (inset) characteristics in the simulated TTJ with two models for the surface charges: self consistent model (SCCM) and *frozen* surface charge profile calculated under equilibrium conditions. The fitting to a parabolic dependence for the two cases is also represented.

FIG. 12. Frequency dependence of the amplitude, V_{Cac}, and average DC value, $\overline{V_C}$, of the response of V_C (normalized to the input amplitude and in dB) to signals of amplitude 100 mV applied in push-pull to the inputs.

FIG. 13. Geometry of the simulated structures. (a) T-shaped junction and (b) Y-shaped junction.

FIG. 14. MC values of (a) bottom potential V_C and (b) current as a function of the push-pull bias obtained in T-shaped junctions with different W_{VER} and W_{HOR} and in a Y-shaped junction (shown in Fig. 13).

FIG. 15. Frequency dependence of (a) amplitude, V_{Cac}, and (b) average DC value, $\overline{V_C}$, of the response of V_C (normalized to the input amplitude and in dB) to signals of amplitude 100 mV applied in push-pull to the inputs in T-shaped junctions with different W_{VER} and W_{HOR} and in a Y-shaped junction (shown in Fig. 13). For a better comparison, the low-frequency value has been subtracted to each curve.

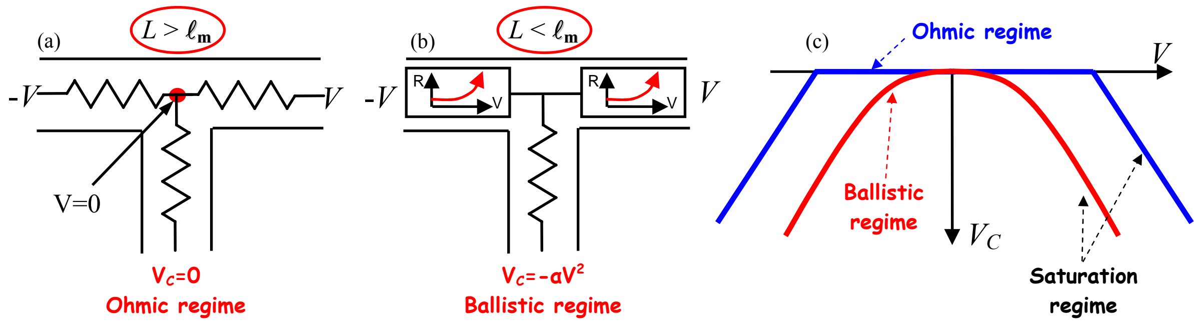

Figure 1

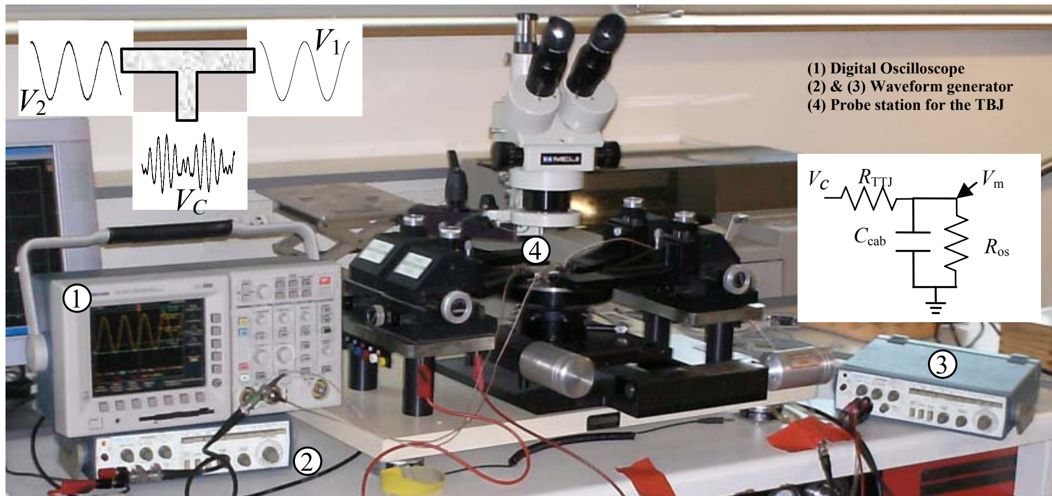

Figure 2

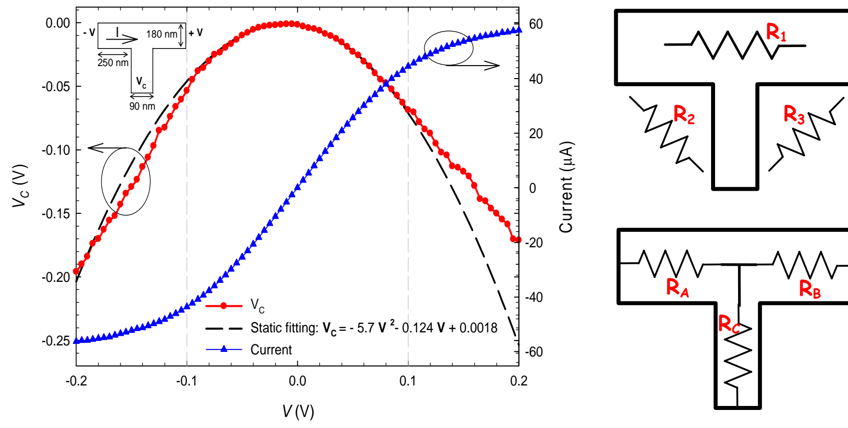

Figure 3

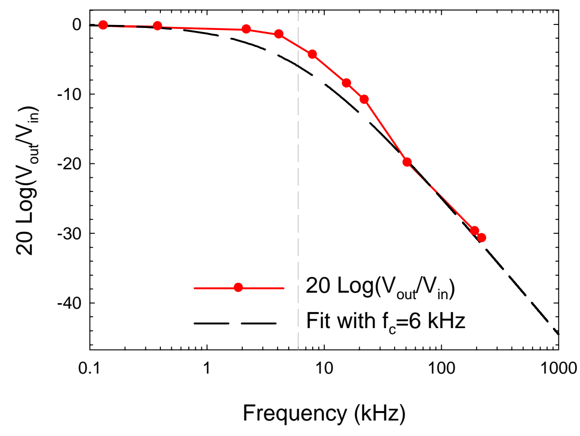

Figure 4

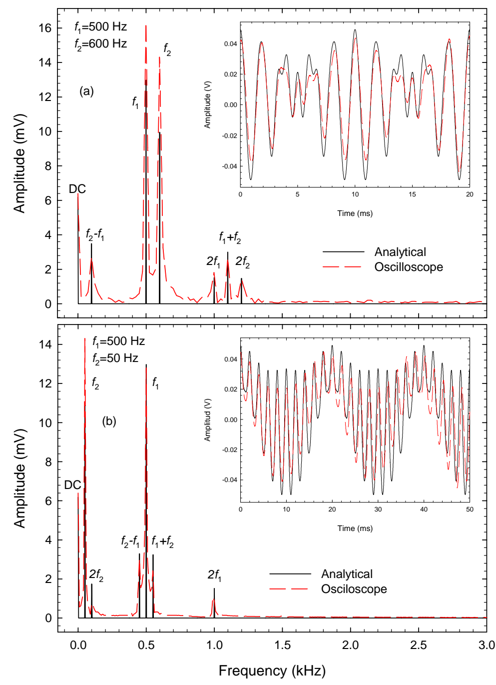

Figure 5

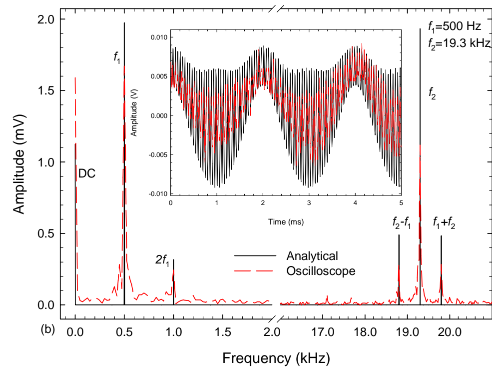

Figure 6

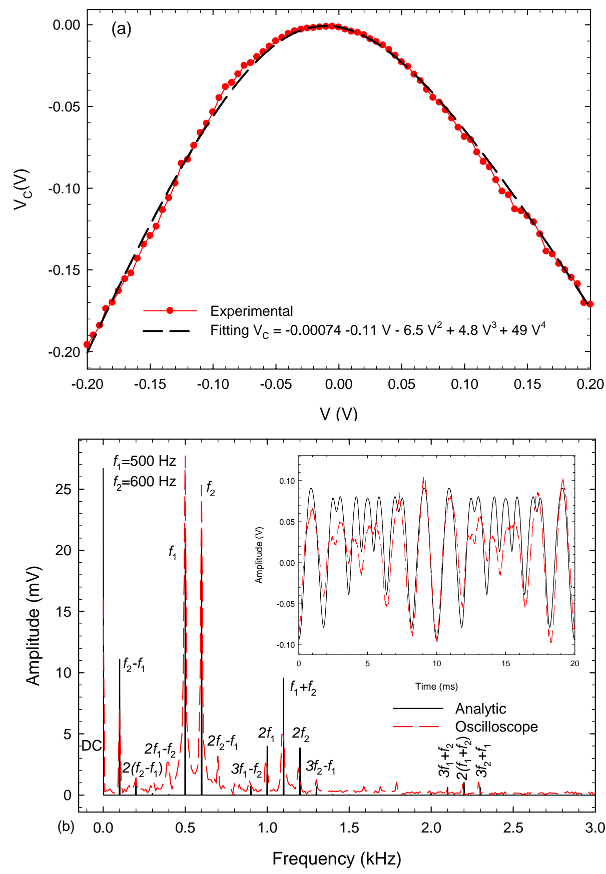

Figure 7

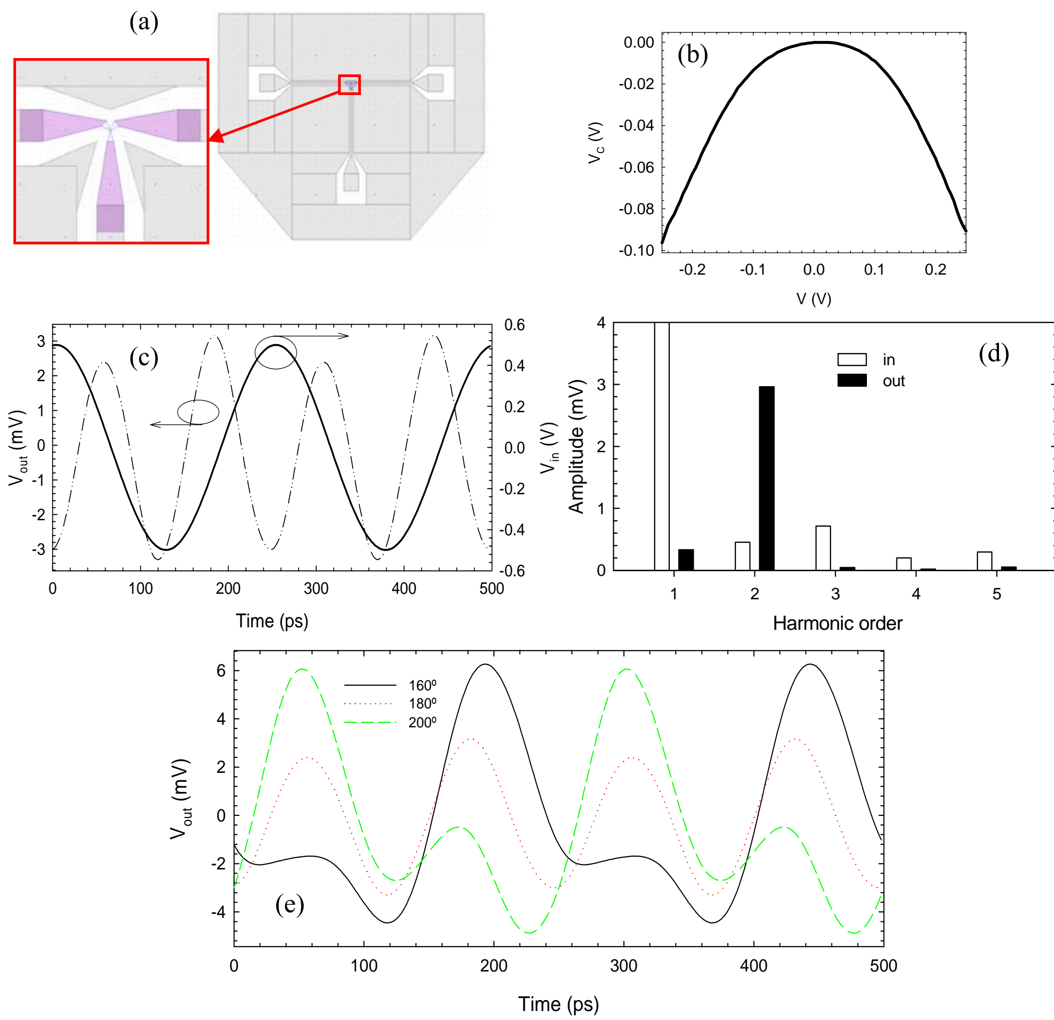

Figure 8

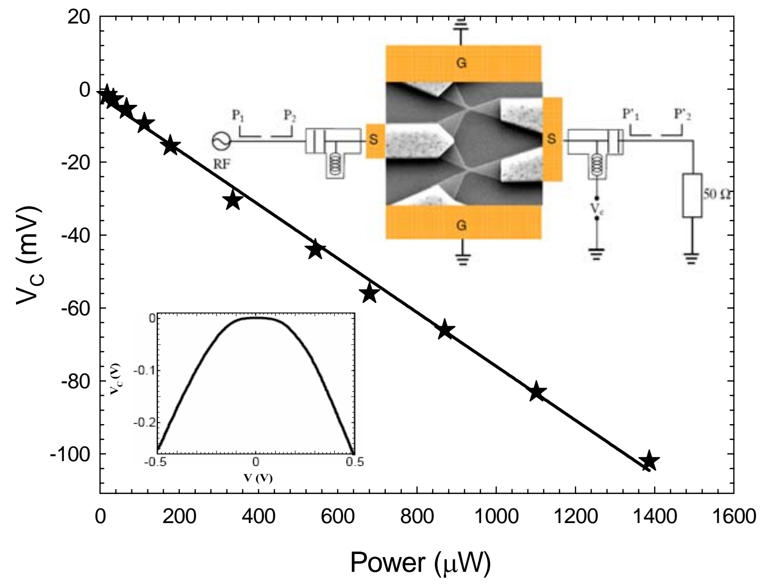

Figure 9

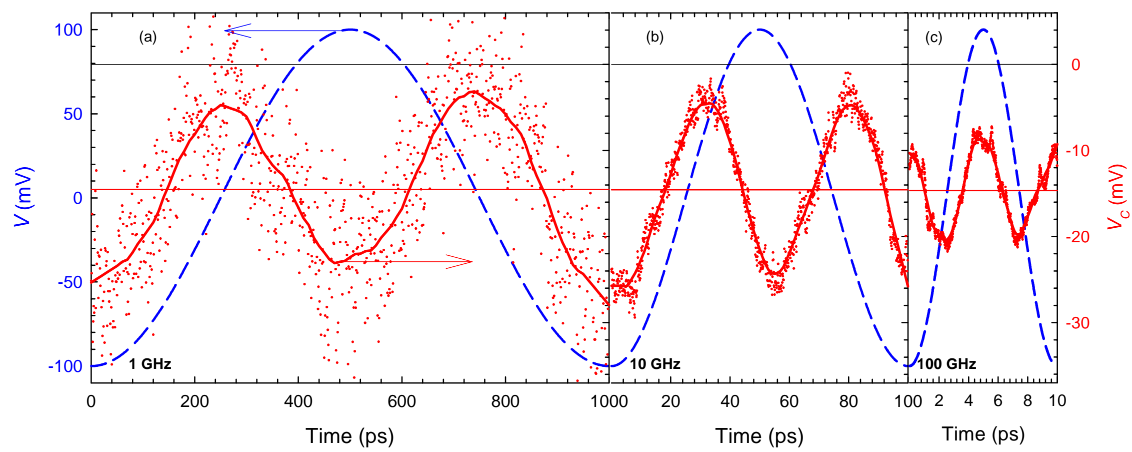

Figure 10

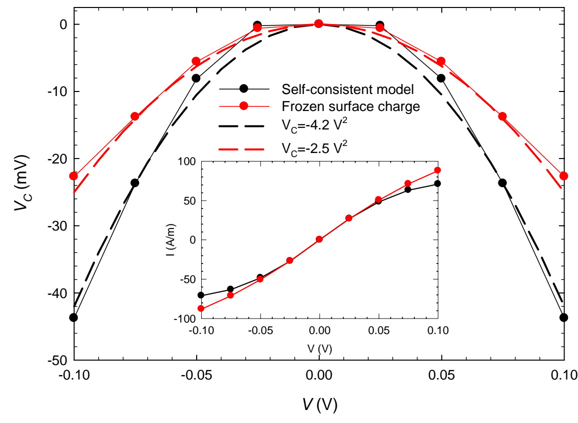

Figure 11

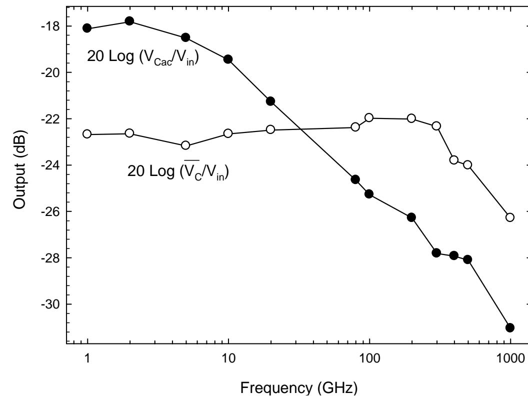

Figure 12

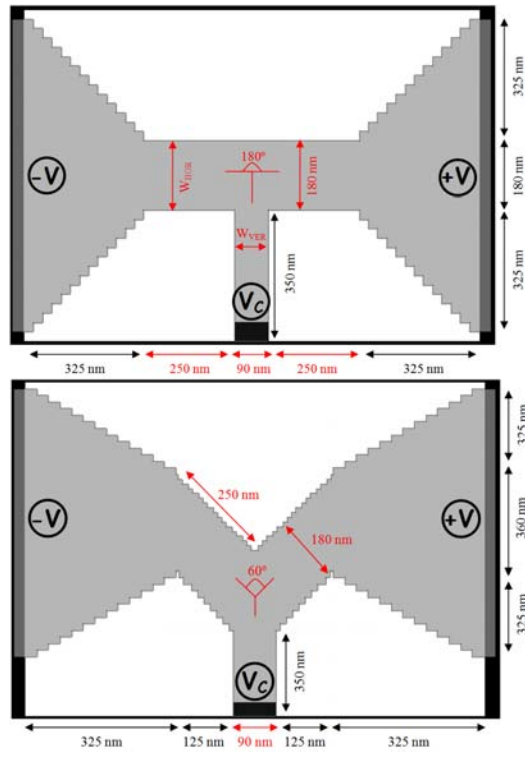

Figure 13

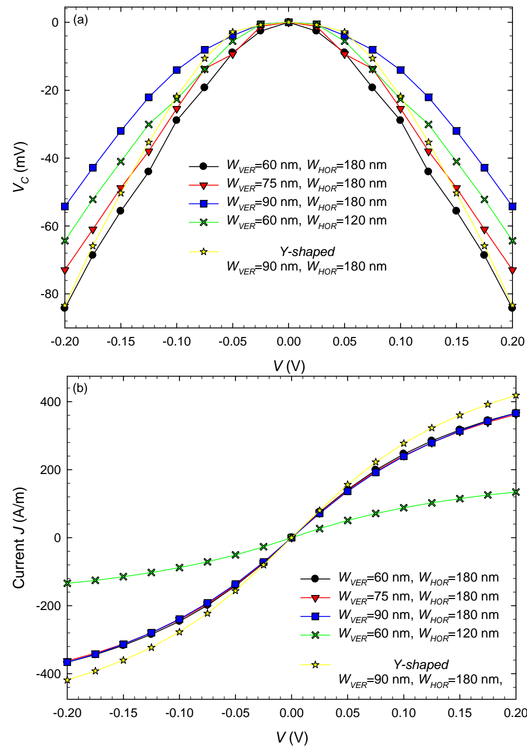

Figure 14

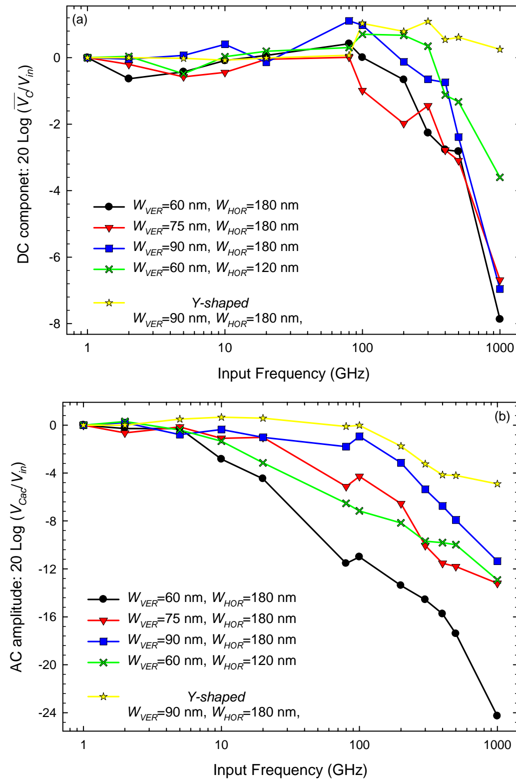

Figure 15